

UNCERTAINTY QUANTIFIED DEEP LEARNING FOR PREDICTING DICE COEFFICIENT OF DIGITAL HISTOPATHOLOGY IMAGE SEGMENTATION

Sambuddha Ghosal[†], Audrey Xie[†], Pratik Shah^{*}

Massachusetts Institute of Technology, Program in Media, Arts and Sciences and Media Laboratory,
20 Ames Street, Cambridge MA 02139, United States

ABSTRACT

Deep learning models (DLMs) can achieve state-of-the-art performance in medical image segmentation and classification tasks. However, DLMs that do not provide feedback for their predictions such as Dice coefficients (Dice) have limited deployment potential in real-world clinical settings. Uncertainty estimates can increase the trust of these automated systems by identifying predictions that need further review but remain computationally prohibitive to deploy. In this study, we use a DLM using randomly initialized weights and Monte Carlo dropout (MCD) to segment tumors from microscopic Hematoxylin and Eosin (H&E) dye stained prostate core biopsy RGB images. We devise a novel approach that uses multiple clinical region-based uncertainties from a single image (instead of the entire image) to predict Dice of the DLM model output by linear models. Image level uncertainty maps were generated and showed correspondence between imperfect model segmentation and high levels of uncertainty associated with specific prostate tissue regions with or without tumors. Results from this study suggest that linear models can learn coefficients of uncertainty quantified deep learning and correlations [Spearman’s correlation ($p < 0.05$)] to predict Dice scores of specific regions of medical images.

Index Terms— Deep learning, Prostate tumor segmentation, Uncertainty based prediction, Statistical modeling

1. INTRODUCTION

Deep neural networks (DNNs) are increasingly used for image detection, classification and segmentation tasks for medical applications [1, 2]. However, these DNN models are considered sub-optimal for real-world clinical applications that require risk-analysis of predictions and associated uncertainty [3]. Many DNNs use softmax [4] as their final activation function to normalize the network output to a probability distribution over each class. However, the resultant probability vector is often incorrectly interpreted as a network confidence. Prior reports have noted that DNNs can produce unjustifiably high confidence for inputs unrelated to

training data [5]. In contrast, a Bayesian perspective neural network provides output and associated uncertainty by placing a distribution over the weights of the trained model [6]. However at the same time, Bayesian methods are prohibitive in terms of computational cost and not feasible for scaling to high-dimensional inputs such as images or videos. Bayesian probability distributions can be learned in a comparatively less expensive manner using linked networks trained with dropout to minimize the Kullback-Leibler divergence between an approximate distribution and the posterior of a deep Gaussian process [5].

1.1. Related Work

Monte Carlo Dropout (MCD) has been used for estimation of uncertainty of predictions from deep learning model performance. A convolutional neural network (CNN) with MCD showed high levels of uncertainty around the edges of target images [7]. That study also reported that class imbalance in training data caused many missed and/or incorrect segmentations [7]. Similar findings were reported in another study for skin lesion segmentation where the deep learning model’s uncertainty distributions were estimated using MCD for different training data classes [8]. Other studies compared uncertainty with a trained deep learning model performance for image segmentation. A linear regression model was used predict a single Dice score of CT scans of the thorax that correlated with image-level uncertainty of segmentation predictions of a deep learning model [9]. However, there are no studies that report relationships, correspondence and contributions between deep learning model uncertainties and segmentation of different clinical regions of interest (ROIs) on medical images (e.g. tumors, tissue structure, non-tissue pixels) and their individual Dice coefficients. Previously reported computational H&E staining of unstained prostate core biopsy images [10] and subsequent classification and segmentation of tumors using deep learning [11], or segmentation of any medical images [12], can benefit from optimizing correspondence between uncertainty-based Dice scores.

[†] equal contribution.

^{*} pratiks@mit.edu – corresponding and senior author.

Table 1: Performance of a deep learning model augmented with Monte-Carlo dropout for tumor segmentation from prostate core biopsy microscopic H&E images with measures of central tendencies of uncertainty estimation. AUROC – Area under the receiver operating characteristic, TPR – True positive rate, FPR – False positive rate, Std. dev. – Standard deviation.

Performance			
Dice	0.8938	TPR	0.8382
AUROC	0.8987	FPR	0.0279
Uncertainty			
Maximum	0.0183	Mean	0.0089
Minimum	0.0016	Std. dev.	0.0042

1.2. Summary of contributions

In this study, a DNN was trained with MCD to calculate model uncertainty at pixel-level uncertainties for segmentation accuracy and reliability of binary segmentation of prostate core biopsy tumors from microscopic H&E stained RGB images. The performance of this MCD model was evaluated using five-fold cross-validation and standard performance metrics (see Methods and Table 1). Using the ground-truth labels all images were further subdivided into three clinical ROIs of pixels with tumors, non-tumor tissue and those without any tissues. Statistically significant ($p < 0.05$) correlations between predictive performance of the MCD model indicated by the Dice was calculated by comparing model output to ground truth segmentation masks for each images. And three individual region-based and overall uncertainty of each image were then calculated. We propose a new algorithm to calculate this region-specific uncertainty (Algorithm 1). Linear models that learned and predicted correspondence between Dice and three clinical region-specific uncertainties derived from MCD model were then trained and validated (Algorithm 1). These linear models could use constants and uncertainty measures for all three clinical ROI individually or in combinations to predict the MCD model performance (Dice) with high accuracy (Eq. 1 and 2). This study reports that although image level uncertainty can be used to estimate Dice (Eq. 3) predictions from a deep learning model, region based uncertainties can provide more specific evaluation of model performance without loss in predictive capabilities and with low Root Mean Square Error (RMSE).

2. DATA DESCRIPTION

Prostate core biopsy images from Gleason2019 (Grand Challenge for Pathology at MICCAI 2019) [13] provides 244 tissue microarray (TMA) 3-channel RGB images of resolution 5120×5120 (W \times H) of H&E dye stained prostate tissue. Each TMA image was annotated in detail by several expert pathologists for assigning a Gleason tumor grade of 1 to 5, and generating Ground-truth (GT) segmentation mask. Gleason grades 1 and 2 are rare and were not associated with tu-

mors and designated as non-tumor tissues along with image pixels without tumors that were represented as black pixels in the GT segmentation mask (class 0). Regions of Gleason Grades 3, 4 and 5 were considered as tumors and represented by white pixels in the GT segmentation mask (class 1). This resulted in 224 images with tumors (Gleason grade 3, 4 or 5), and 20 images without tumors. Detailed description on data pre-processing and training of deep learning models with five-fold cross validation have been previously described in [12].

3. METHODS

A Bayesian VGG-UNet CNN augmented by MCD was trained using prostate core biopsy images and their labels generated from the Grand Challenge for Pathology at MICCAI 2019 [13] as described in this section. The network consists of an encoder-decoder structure [14], where the encoder portion uses a modified version of the VGG-16 architecture [15] that lacks the fully-connected layers. Uncertainty quantification was implemented from the decoder to mitigate noise that could disrupt information transfer during the down-scaling (encoding) step. Uncertainty estimations using MCD were used to approximate Bayesian inference that minimized an approximate posterior within a deep Gaussian Process (GP) [5].

3.1. Model training

The prostate core biopsy data was split into 80% for training (≈ 197 images) and 20% for testing (≈ 47 images). The model was trained for 50 epochs with a batch size of two and the Adam optimizer with learning rate set at $\alpha_{lr} = 0.001$ was used. Model input images were resized to 1024×1024 (W \times H) while outputs from the trained model were kept at 512×512 (W \times H). Model training and evaluation was carried out using NVIDIA GeForce RTX 2080 Ti with 11GB of GPU memory.

3.2. Model prediction and evaluation

For each model prediction, the number of True Positive (TP), False Positive (FP), False Negative (FN), and True Negative (TN) pixels were counted over the entire output. A TP instance was when a tumor pixel was segmented accurately, TN when a non-tumor or non-tissue pixel was not segmented. False negative pixels were those that were not segmented by the model, but were denoted as tumor pixels in the ground truth, and FP pixels were those segmented as a tumor by the model but classified as non-tumor tissue or non-tissue in the ground truth data. Using these definitions, we calculated four metrics - the True Positive Rate (TPR) and False Positive Rate (FPR) for model predictions for all the images in the test data, and the AUROC and Dice that evaluated the similarity between the ground truth clinical labels and model generated

Algorithm 1 ROI-Unc: Modelling performance based on region specific uncertainty

Step 1: Model predictions and associated uncertainty maps

Input: Optimized and trained MCD model, M ; Test data, X_{test} with n images and corresponding labels (ground-truth), X_{GT} .

Output: Model segmentation output, O_{M_i} and uncertainty map, Unc_{map_i} (see Methods Section 3.2) corresponding to X_{test_i} . Thus, $\forall i = [1, 2, \dots, n]$ images,

$$X_{Dice_i} = Dice(O_{M_i}, X_{GT_i}), List_{Dice} = [X_{Dice_i}]_{i=1}^n, List_{Unc} = [Unc_{map_i}]_{i=1}^n$$

Step 2: Generate ROI uncertainty:

Input: Given a test image, X_{test_i} and a corresponding ground-truth mask, X_{GT_i} , we generated the following:

- X_{test_i} -bin: a binary transformation of the input RGB image with a value of '0' representing pixels of non-tissue pixels without any tissue regions and '1' ('255' in grayscale) representing tissue regions with or without tumors.
- X_{test_i} -tumor = X_{GT_i}
- X_{test_i} -non-tumor = difference(X_{test_i} -bin, X_{test_i} -tumor)
- X_{test_i} -bin^C: complement of X_{test_i} -bin or, a binary representation of the input image with a value of '1' ('255' in grayscale) representing non-tissue regions and '0' representing tissue regions.

Output: Uncertainty maps corresponding to these specific regions are generated as follows:

- $Unc_{i_T} = Unc_{test_i}$ -tumor = (X_{test_i} -tumor \odot Unc_{map_i}); $List_{T_{unc}} = [mean(Unc_{i_T})]_{i=1}^n$.
- $Unc_{i_{NT}} = Unc_{test_i}$ -non-tumor = (X_{test_i} -non-tumor \odot Unc_{map_i}); $List_{NT_{unc}} = [mean(Unc_{i_{NT}})]_{i=1}^n$.
- $Unc_{i_{NTi}} = Unc_{test_i}$ -non-tissue = (X_{test_i} -bin^C \odot Unc_{map_i}); $List_{NTi_{unc}} = [mean(Unc_{i_{NTi}})]_{i=1}^n$. The symbol \odot represents the Hadamard product.

Step 3: Generate linear regression models:

Input: Dependent variable, $List_{Dice} = Y_{Dice}$ (say) = $[y_{Dice_i}]_{i=1}^n$ for n images, and independent variables:

- $List_{Unc} = X_0$ (say) = $[x_{0i}]_{i=1}^n$ (corresponds to the overall uncertainty maps as shown in Supp. Fig. S1 column D),
- $List_{T_{unc}} = X_1$ (say) = $[x_{1i}]_{i=1}^n$ (tumor tissue uncertainty maps as shown in Supp. Fig. S1 column E),
- $List_{NT_{unc}} = X_2$ (say) = $[x_{2i}]_{i=1}^n$ (non-tumor tissue uncertainty maps as shown in Supp. Fig. S1 column F) and
- $List_{NTi_{unc}} = X_3$ (say) = $[x_{3i}]_{i=1}^n$ (uncertainty maps for non-tissue pixels without tissue as shown in Supp. Fig. S1 column G) – that predict Y_{Dice} , where n is the total number of images under consideration.

Output: Model Y_{Dice} in terms of X_1 , X_2 and X_3 as follows:

$$Y_{Dice} = \alpha_0 + \alpha_1 * X_1 + \alpha_2 * X_2 + \alpha_3 * X_3 \quad (1)$$

For individual ROIs:

$$(i) Y_{Dice} = \beta_0 + \beta_1 * X_1, \quad (ii) Y_{Dice} = \gamma_0 + \gamma_1 * X_2, \quad (iii) Y_{Dice} = \delta_0 + \delta_1 * X_3. \quad (2)$$

and for the overall uncertainty, X_0 :

$$Y_{Dice} = \theta_a + \theta_b * X_0 \quad (3)$$

segmentation. Dice was used for subsequent liner model estimations. Overall median Dice, AUROC, TPR and FPR values for all 47 test images are reported in (**Table 1**). For each image, a distribution of pixel-level uncertainty was obtained as well. From these distributions, we calculated central tendencies for image-specific mean uncertainty. Using these individual mean uncertainty values, we report the overall mean uncertainty for all 47 test images in Table 1. Uncertainty estimates resulting from this evaluation range between a minimum value of 0 for the model being fully certain of its prediction to a maximum of 1 when the model is fully uncertain about its prediction. To obtain pixel-level uncertainty, 50 MC iterations were taken where the difference between 67th and 33rd percentiles of their sigmoid values from the model's pre-

dictions were set as uncertainty estimates and represented as heatmaps (Supp. Fig. S1) and in Table 1.

Mathematically, for a given MCD model M and input test image X_{test_i} , the model prediction was calculated by: $O_{M_p}^j = \text{argmax}(M_p(X_{test_i}))$ for the j^{th} MC iteration, where M_p is the model M in testing phase. The final model output O_{M_i} was generated by taking a mean of all 50 MC iteration outputs. To generate the predicted segmentation outputs, a value based thresholding was used to designate the predicted class to which the pixel belonged. Predicted 'class 0' (pixel value of '0' in binary scale) or non-tumor pixels were assigned a value of 0 only if the mean value for the corresponding pixel across all MC iterations was ≤ 0.95 , and predicted 'class 1' (pixel value of '1' in binary scale) or tumor pixels as 1 were

assigned only if the mean value from the MC iterations was > 0.95 . Thus,

$$O_{M_{p1}} = 1/\alpha \sum_{j=1}^{\alpha} O_{M_p}^j \quad (4)$$

where $\alpha = 50$ is the number of MC iterations. And, the final model output, $O_{M_i} = [O_{M_{p1}} \text{ s.t } \forall \text{ pixels, } p \text{ in } O_{M_{p1}}, (|p| > 0.95) \implies (|p| = 1) \text{ and } (|p| \leq 0.95) \implies (|p| = 0)]$. To obtain the corresponding uncertainty map, Unc_{map_i} , we note that each MC iteration step produced an uncertainty map as $Unc_{M_p}^j = \max(M_p(X_{test_i}))$. Thus,

$$Unc_{map_i} = P_{67}([Unc_{M_p}^j]_{j=1}^{\alpha}) - P_{33}([Unc_{M_p}^j]_{j=1}^{\alpha}) \quad (5)$$

4. RESULTS AND DISCUSSION

4.1. MCD model performance and uncertainty

Five-fold cross-validation was used for segmentation of prostate tumors and estimating segmentation uncertainties of the trained MCD model. Values for AUROC were [0.8938 (95% CI: 0.8582 - 0.9019)], Dice [0.8987 (95% CI: 0.8561 – 0.9095)], TPR [0.8382 (95% CI: 0.7792 - 0.8980)] and FPR [0.0279 (95% CI: 0.0296 -0.0829)] (confidence intervals, CI were calculated using the empirical bootstrap method with $n = 5,000$ simulations). These results indicated that the MCD model achieved high performance (Table 1) for prostate tumor segmentation. We note that the overall uncertainty prediction were on the lower end (less than 1%). However, individual ROI within an input image reached uncertainties as high as 20% (Supp. Fig. S1).

4.2. Modelling performance based on uncertainty

We propose Algorithm 1 to calculated estimated performance (Dice) of a model using uncertainties for clinical ROIs in a medical image. Eq. 1 calculated the Dice of the segmentation model based on a linear combination of tumor-tissue, non-tumor tissue and non-tissue uncertainties, and equations 2(i), 2(ii) and 2(iii) calculated the Dice of the segmentation model from the three individual ROIs. Two subsets of test data were used for calculating linear models and for obtaining the values of the coefficients for equations 1 to 3 and are described below:

4.2.1. Tumor-containing images

Forty four images that contained tumor labels from the test data set were used as the first subset. From these tumor containing images, we obtained $\alpha_0 = 1.0036$, $\alpha_1 = -12.2397$, $\alpha_2 = -19.5844$ and $\alpha_3 = -6.2364$; for tumor uncertainty (Spearman's correlation coefficient (ρ) = -0.4878), $\beta_0 = 0.9264$ and $\beta_1 = -7.9295$; for non-tumor uncertainty (ρ = -0.5012), $\gamma_0 = 0.9011$ and $\gamma_1 = -13.9173$; for non-tissue uncertainty (ρ = -0.5969), $\delta_0 = 0.9702$ and $\delta_1 = -26.9116$, and for the overall

uncertainty (ρ = -0.8496), $\theta_a = 1.0074$ and $\theta_b = -14.9116$. Low RMSE of ≤ 0.1 was calculated for all five linear models for the tumor containing images.

4.2.2. Tumor-free images

Three images from the test data and 17 images from the training data that did not contain any tumor labels were merged into the second subset. From these tumor-free images we obtained $\alpha_0 = 0.9991$, $\alpha_1 = 0$ (which is expected since the tumor regions did not contribute to the model uncertainties or performance), $\alpha_2 = -12.306$ and $\alpha_3 = 7.2247$; for non-tumor uncertainty (ρ = -0.8496), $\gamma_0 = 0.9993$ and $\gamma_1 = -8.5907$; for non-tissue uncertainty (ρ = -0.8496), $\delta_0 = 0.9993$ and $\delta_1 = -16.02$, and for the overall uncertainty (ρ = -0.8496), $\theta_a = 0.9994$ and $\theta_b = -5.6296$. The RMSE values for the tumor-free images for all four linear models were even lower at 0.014. For all derived coefficients, except for α_3 for the tumor-free images, negative coefficient values indicated that uncertainty in the MCD model predictions decreased its performance.

From the coefficients derived for Eq. 1 we further note the importance of each clinical region to models overall performance. A lesser (more negative) value of the coefficient implying a greater contribution in reducing Dice. For the tumor containing images, we report non-tumor tissue region uncertainties had the highest coefficient value (weight) relative to the other regions. These results also indicated that the MCD model performance was most affected (reduced) by uncertainty of predictions of non-tumor tissue, followed by the tumor-tissue regions, and non-tissue pixels contributed approximately half as much as the tumor regions. For the tumor-free images, non-tumor tissue regions uncertainty contributed more substantially than pixels without any tissue (indicated by a positive α_3 coefficient).

5. CONCLUSION AND LIMITATIONS

We report that clinical region-based linear models could predict deep learning model performance (Dice) using either individual or combination of uncertainty estimations (equations. 1 - 3). Other studies have reported such relationships only between Dice and overall uncertainty measures. To the best of our knowledge, we are the first to derive clinically meaningful and actionable insights by leveraging tissue features within the training data for estimating and correlating Bayesian deep learning model performance with uncertainty estimates. This study also decoupled three different clinical and region-based uncertainty estimates for the first time for prostate tumors. Spearman's rank correlation (ρ) was used to establish significance ($p < 0.05$) between overall and ROI-based uncertainties with MCD model performance of Dice. A high negative value obtained for all regions indicated that a strong negative correlation exists between uncertainty and model performance. Coefficients determined through linear

regression for these regions also supported this finding, with almost all coefficients having a negative value (except α_3 for the Tumor-free images). A low RMSE indicated goodness of fit for these results. Equation 1 can predict performance based on all three regions simultaneously, and the value of its coefficients can identify which regions of the image may contribute to greater uncertainty thereby leading to poor model performance. A key aspect of equations 1 and 2 is that, given the ROI-based uncertainty measure it was possible to obtain the model performance value. For e.g., given a trained deep learning model, one can use Algorithm 1 for estimating model performance of Dice in an unsupervised manner, corresponding uncertainty maps and mean uncertainty values. Using these methods, a deep learning model with or without MCD and with least uncertainty in its prediction and highest possible accuracy for clinical ROIs can be trained and optimized. Clinical ROI-based uncertainty estimates along with predicted model performance measures such as Dice obtained by the proposed algorithm and linear models can be leveraged to make informed decisions in real-world clinical situations. The results and conclusions from this study are currently limited to the prostate core biopsy image data set, MCD and Dice as parameters. Other data sets, uncertainty estimation methods such as Bayes-by-backprop and model performance metrics such as AUROC, TPR and FPR are a future growth area from this research.

6. REFERENCES

- [1] June-Goo Lee, Sanghoon Jun, Young-Won Cho, Hyunna Lee, Guk Bae Kim, Joon Beom Seo, and Namkug Kim, "Deep learning in medical imaging: general overview," *Korean journal of radiology*, vol. 18, no. 4, pp. 570–584, 2017.
- [2] Geert Litjens, Thijs Kooi, Babak Ehteshami Bejnordi, Arnaud Arindra Adiyoso Setio, Francesco Ciompi, Mohsen Ghahfarouh, Jeroen AWM Van Der Laak, Bram Van Ginneken, and Clara I Sánchez, "A survey on deep learning in medical image analysis," *Medical image analysis*, vol. 42, pp. 60–88, 2017.
- [3] Garry Choy, Omid Khalilzadeh, Mark Michalski, Synho Do, Anthony E Samir, Oleg S Pinykh, J Raymond Geis, Pari V Pandharipande, James A Brink, and Keith J Dreyer, "Current applications and future impact of machine learning in radiology," *Radiology*, vol. 288, no. 2, pp. 318–328, 2018.
- [4] John S Bridle, "Training stochastic model recognition algorithms as networks can lead to maximum mutual information estimation of parameters," in *Advances in neural information processing systems*, 1990, pp. 211–217.
- [5] Yariv Gal and Zoubin Ghahramani, "Dropout as a bayesian approximation: Representing model uncertainty in deep learning," in *international conference on machine learning*. PMLR, 2016, pp. 1050–1059.
- [6] Christopher M Bishop, "Bayesian neural networks," *Journal of the Brazilian Computer Society*, vol. 4, pp. 61–68, 1997.
- [7] Michael Kampffmeyer, Arnt-Borre Salberg, and Robert Jenssen, "Semantic segmentation of small objects and modeling of uncertainty in urban remote sensing images using deep convolutional neural networks," in *Proceedings of the IEEE conference on computer vision and pattern recognition workshops*, 2016, pp. 1–9.
- [8] Pieter Van Molle, Tim Verbelen, Cedric De Boom, Bert Vankeirsbilck, Jonas De Vylder, Bart Diricx, Tom Kimpe, Pieter Simoens, and Bart Dhoedt, "Quantifying uncertainty of deep neural networks in skin lesion classification," in *Uncertainty for Safe Utilization of Machine Learning in Medical Imaging and Clinical Image-Based Procedures*, pp. 52–61. Springer, 2019.
- [9] Katharina Hoebel, Vincent Andrearczyk, Andrew Beers, Jay Patel, Ken Chang, Adrien Depeursinge, Henning Müller, and Jayashree Kalpathy-Cramer, "An exploration of uncertainty information for segmentation quality assessment," in *Medical Imaging 2020: Image Processing*. International Society for Optics and Photonics, 2020, vol. 11313, p. 113131K.
- [10] Multiple Authors first Names Multiple Authors Last Names, "paper title," *Journal Name*, vol. **, no. **, pp. ****, 2020.
- [11] First names Author Last, "Paper title," in *Book Title*. **** Society, 2021, vol. vol, p. pages.
- [12] Author 1 Name Author 1 Surname and Author 2 Name Author 2 Surname, "Paper title ****," *Paper Link* ****, 2020.
- [13] "Gleason 2019 homepage," 2019, <https://gleason2019.grand-challenge.org/>.
- [14] Olaf Ronneberger, Philipp Fischer, and Thomas Brox, "U-net: Convolutional networks for biomedical image segmentation," in *International Conference on Medical image computing and computer-assisted intervention*. Springer, 2015, pp. 234–241.
- [15] Karen Simonyan and Andrew Zisserman, "Very deep convolutional networks for large-scale image recognition," *arXiv preprint arXiv:1409.1556*, 2014.

Ethical compliance: This research study was conducted retrospectively using human subject data made available in open access by <https://gleason2019.grand-challenge.org/>. Ethical approval was not required as confirmed by the license attached with the open access data.

Conflicts of interest: The authors have no relevant financial or non-financial interests to disclose.

SUPPLEMENTARY INFORMATION

1. INTRODUCTION

Figure S1 shows input images and the corresponding GT masks from six representative images. To obtain pixel-level uncertainty, 50 MC iterations were taken where the difference between 67th and 33rd percentiles of their sigmoid values from the model’s predictions were set as uncertainty estimates and represented as heatmaps (Fig. S1).

2. RESULTS AND DISCUSSION

2.1. Model performance and uncertainty

We note that the overall uncertainty prediction were on the lower end (less than 1%). However, certain regions within an input image reached uncertainties as high as 20% (Fig. S1).

2.2. Qualitative evaluation

Figure S1 shows four tumor containing and two non-tumor prostate images from the test data and MCD model output segmentation masks and corresponding uncertainty heatmaps from the trained model. Model predictions O_{M_i} and overall uncertainty map, Unc_{map_i} obtained using step 2 of Algorithm 1 are shown in columns C and D respectively. The region based uncertainty maps generated using step 2 of Algorithm 1, Unc_{i_T} , $Unc_{i_{NT}}$ and $Unc_{i_{NTi}}$ are shown in columns E, F and G respectively. Images 1 to 4 contained tumors and images 5 and 6 did not contain ground-truth tumor signatures. Predictions for images 1 and 2 exhibited almost no false positive or false negative regions, images 3 and 4 showed low false positives and good segmentation accuracy. Images 5 and 6 exhibited the highest false positive regions as such examples were less frequent in the training data compared to images that had tumors in them. Overall uncertainty maps (column D) also showed that images that had tumors all throughout the tissue regions (images 1 and 2) exhibited the least uncertainty. Majority of the detected uncertainty for these images were at the tissue and non-tissue boundary regions. The model showed no uncertainties in the non-tissue regions except for the junction between tissue and non-tissue regions. This indicated that the model has learnt the non-tissue region well and is uncertain at the non-tissue

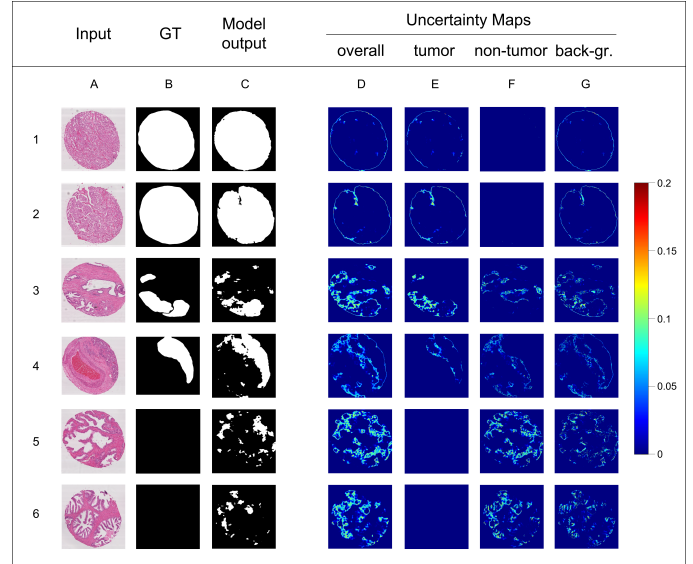


Fig. S1: Model output segmentation and region-based uncertainty maps. Visualization of model output and uncertainty explanations for prostate tumor segmentation by a Monte Carlo dropout deep learning model (MCD) trained using microscopic Hematoxylin and Eosin (H&E) dye stained prostate core biopsy images. **Left to right columns:** A, Input RGB image; B, Binary mask of clinical ground-truth label; C, Binary mask of segmentation from MCD output image; D, Uncertainty estimate maps of binary segmentation of MCD model; E, Uncertainty estimate maps of binary segmentation of MCD model for tumor tissue regions; F, Uncertainty estimate map of binary segmentation of MCD model for non-tumor tissue regions; G, Uncertainty estimate map of MCD model binary segmentation for non-tissue regions. Color bar shows the degree of model uncertainty with deeper red indicating greater uncertainty and deeper blue indicating the least uncertainty (with lowest value being 0). “GT” – clinical ground-truth, “back-gr” – non-tissue regions.

and tissue junctions and more frequently at the non-tumor tissue and tumor tissue region intersections. This was especially true for those regions indicated by the ground-truth as containing tumorous tissues in images 2 and 3. For images 5 and 6 the absence of tumors gives the tissue island like appearance – which may lead to a greater degree of confusion for the model and non-tumor tissue uncertainty. Visualizing these individual ROI-based uncertainty maps (Fig. S1), also helped in identifying regions of high uncertainties and make informed decisions on whether to discard a model’s output or not based on where the higher uncertainties arose from. For example in image 3 in Fig. S1, high uncertainties were observed in the tumor region indicating that the model may show poor performance within tumor regions in similar images during inference, while similar uncertainties were observed in image 2 for the tumor and non-tissue regions – indicating that predictions may be acceptable for cases when differential diagnosis depended on disease pixels.